Journal of Instrumentation

SISSA

PAPER • OPEN ACCESS

Magnetic triggering — time-resolved characterisation of silicon strip modules in the presence of switching DC-DC converters

To cite this article: A.J. Blue *et al* 2021 *JINST* **16** P06012

Published by IOP Publishing for Sissa Medialab

Received: *February 18, 2021*
Accepted: *March 3, 2021*
Published: *June 16, 2021*

Magnetic triggering — time-resolved characterisation of silicon strip modules in the presence of switching DC-DC converters

A.J. Blue,[a] B. Gallop,[b] T. Heim,[c] C. Helling,[d] K. Krizka,[c] B. Li,[c,e] C. Labitan,[c] E. Mladina,[c] L. Poley,[f,g,1,*] P.W. Phillips,[b] S.N. Santpur[c] and C.A. Sawyer[b,*]

[a] *SUPA School of Physics and Astronomy, University of Glasgow, University Avenue, Glasgow, U.K.*
[b] *Particle Physics Department, STFC Rutherford Appleton Laboratory, Harwell Science and Innovation Campus, Didcot, U.K.*
[c] *Lawrence Berkeley National Laboratory, Cyclotron Road, Berkeley, U.S.A.*
[d] *Institute of Particle Physics, University of California, High Street, Santa Cruz, U.S.A.*
[e] *Department of Physics, Tsinghua University, Beijing, China*
[f] *Department of Physics, Simon Fraser University, University Dr W, Burnaby, Canada*
[g] *TRIUMF, Wesbrook Mall, Vancouver, Canada*

E-mail: Craig.Sawyer@stfc.ac.uk, LPoley@triumf.ca

Abstract: Modules for the ATLAS Inner Tracker (ITk) strip tracker include a DC-DC converter circuit glued directly to the silicon sensor which converts the 11 V supplied to the module to the 1.5 V required for the operation of the readout chips. The DC-DC converter unit, consisting of a copper solenoid and custom ASIC, is located directly above the silicon strip sensor and therefore needs to be shielded to protect the sensor from EMI noise created during the operation of the circuit. Despite dedicated shielding, consisting of an aluminium shield box with continuous solder seams encompassing the surface components and a copper layer in the PCB beneath it, module channels connected to sensor strips located beneath the converter circuit were found to show a noise increase. While the DC-DC converter unit causing the underlying EMI noise operates at a frequency of 2 MHz, module characterisation measurements for ITk strip tracker modules are typically performed asynchronously to the DC-DC switching and are therefore averaged over the full range of time bins with respect to the converter frequency. In order to investigate the time dependence of the noise injection relative to the DC-DC switching frequency, a dedicated setup to understand the time-resolved performance change in modules was developed. By using a magnetic field probe

*Corresponding authors.
[1] Previous affiliation: Lawrence Berkeley National Laboratory, Cyclotron Road, Berkeley, U.S.A.

https://doi.org/10.1088/1748-0221/16/06/P06012

to measure the field leaking through the shield box and triggering on its rising edge, data taking could be synchronised with the DC-DC switching. This paper illustrates the concept and setup of such time-resolved performance measurements using magnetic triggering and presents results for the observed effects on signal and noise for ATLAS ITk strip modules from both laboratory and beam tests.

KEYWORDS: Data acquisition concepts; Digital electronic circuits; Particle tracking detectors; Si microstrip and pad detectors

2021 JINST 16 P06012

Contents

1 Introduction

Modules for the future ATLAS strip tracker [1] consist of a $10 \times 10\,\mathrm{cm}^2$ silicon strip sensor onto which one or two hybrids and one powerboard are glued [2]. The hybrids support the readout chips, whereas the powerboard provides four main functions:

- Converting the 11 V supply voltage down to 1.5 V to power the readout chips on the hybrid(s)
- Switching and monitoring the high voltage (up to −500 V) supply to the sensor
- Controlling and monitoring the LV supplied to the module
- Monitoring the powerboard and hybrid temperatures via negative temperature coefficient (NTC) thermistors and active on-chip structures.

The DC-DC regulation of the module is performed by a custom-developed ASIC called FEAST [3] in combination with an external inductance provided by a copper solenoid coil [2]. The position and shape of the coil cause the emission of EMI noise, which can cause an increased noise in sensor areas located beneath the coil. The solenoidal copper coil, ASIC and switching nodes are enclosed by a gold-plated aluminium shield box with continuous solder seams which, combined with the dedicated copper layer in the powerboard flex, form a Faraday cage. Despite this dedicated shielding, sensor areas located below the powerboard shield box on prototype silicon strip sensor modules exhibited an increased input noise.

ABC front-end ASICs operate in binary readout; therefore noise measurements are typically performed by applying a fit to S-curves obtained for individual module channels triggering asynchronously with the switching of the DC-DC regulator. It should be noted that results from this asynchronous data taking mode, used in characterisation tests and anticipated for the HL-LHC,

2021 JINST 16 P06012

complied with module performance requirements [2], but are smeared over the full range of latencies between DC-DC switching and triggering and therefore average over any time-dependent effects. Since the noise increase was assumed to be caused by the EMI noise emitted from the DC-DC circuitry, an additional time-resolved study of the observed noise increase and the DC-DC switching was performed.

In order to perform such measurements, a method was developed to trigger on the magnetic field emitted from the DC-DC circuit and measure the variation in module performance as a function of the phase between the trigger and the DC-DC switch. It should be noted that the parameter of most interest for detector design is the signal-to-noise ratio. For the ITk strip detector, the signal-to-noise ratio is specified to be above 10 at end-of-life (before radiation damage, the signal-to-noise is significantly higher than this). As the LHC runs asynchronously to the DC-DC switching frequency, this specification must be satisfied in all time-bins within the DC-DC cycle.

The module used in these studies is a "long-strip" (strip length of about 5 cm) module built from prototype ASICs of the "star" generation (ABCstar) which are very close to the final chipset expected to be installed in the detector [4]. The module uses an ATLAS17-LS sensor, which has only minor differences from the final long-strip sensor design [5]. Figure 1 shows an annotated image of the module used.

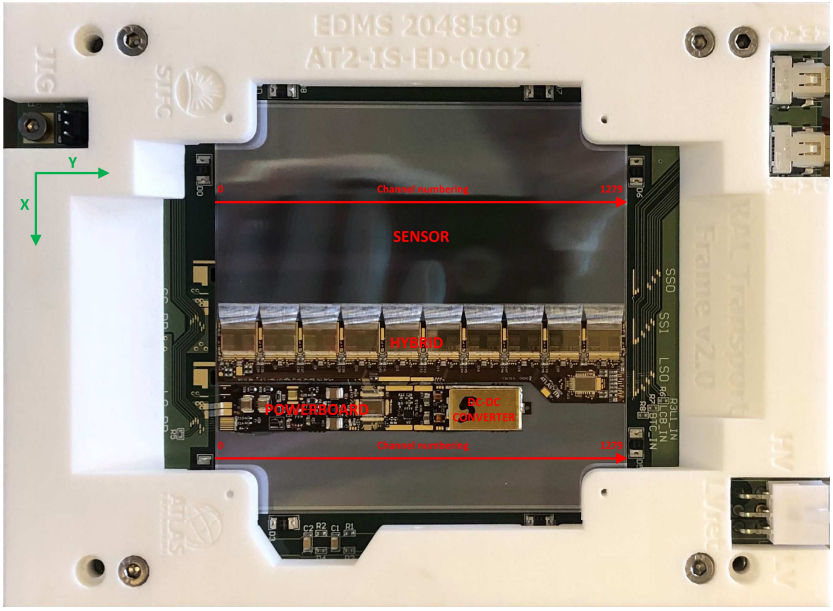

Figure 1. Annotated image of the long-strip module used in these studies. There are two segments of 1280 5 cm strips on the sensor, one bank of which runs away from the hybrid and one bank of which runs under the hybrid and powerboard. The channel numbering from 0 to 1279 for the two strip segments is included on the diagram along with the x- and y-axes as defined in the beam tests.

The method by which data taking was synchronised with the switching of the DC-DC circuit is described in section 2; section 3 describes the use of such a setup with a micro-focused X-ray beam. Sections 4 and 5 outline the measurements performed and the results. Section 6 explains how

2021 JINST 16 P06012

these results can be extrapolated to end-of-life running of modules in the detector itself. Finally, the outlook and proposed future measurements are discussed in section 7.

2 Magnetic triggering

Although the shield box is designed to act as a Faraday cage and reduce EMI emissions, it cannot fully shield the *B*-field emissions (*B*-field shielding primarily arises from induced eddy currents within the Faraday cage). As can be seen in figure 2, the shield box is very effective in shielding *E*-field emissions but does not fully eliminate *B*-field leakage. As a result, the use of a suitably sensitive *B*-field probe can provide a live measurement of the switching of the DC-DC converter and thereby can be used to run data taking synchronously to the DC-DC converter.

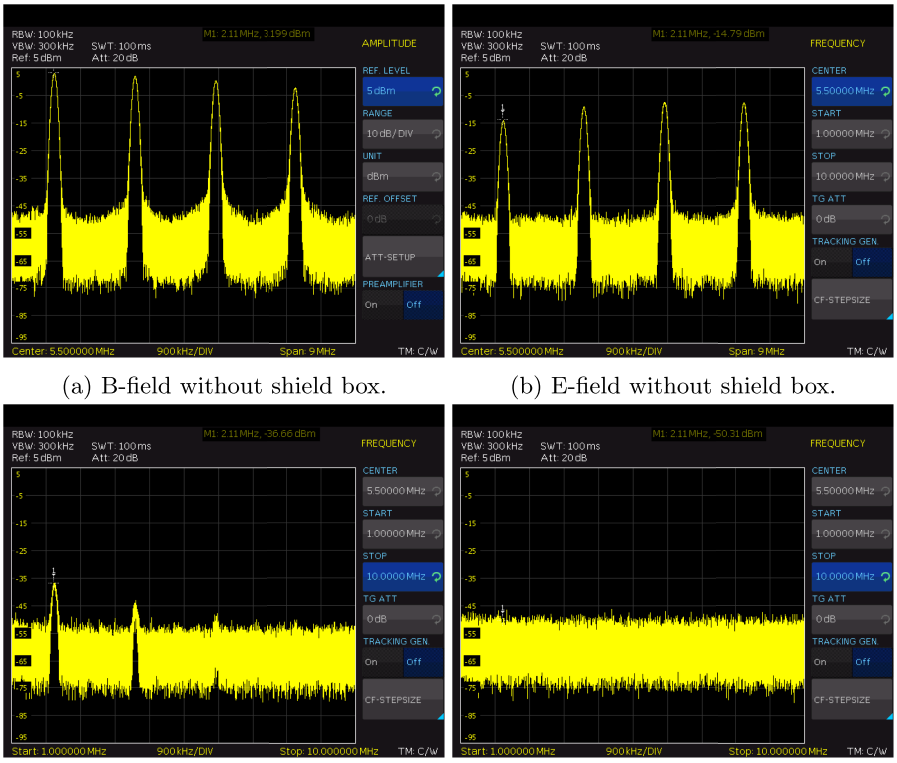

(a) B-field without shield box.

(b) E-field without shield box.

(c) B-field with shield box.

(d) E-field with shield box.

Figure 2. Measured frequency spectra using *E*- and *B*-field probes for the case where there is no shield box above the powerboard coil and where there is a fully soldered shield box in place. Probes are held above the centre of the coil in all cases.

A schematic of the setup used to run synchronous data taking is shown in figure 3; the positioning of the magnetic field probe over a module can be seen in figure 4. The magnetic field probe is held above the module such that the centre of the probe coil approximately lines up with the centre of the coil on the powerboard (the orientation of the solenoid coil on the powerboard can be seen in figure 9). The signal from the probe is then sent through a radio frequency (RF)

2021 JINST 16 P06012

amplifier and into an oscilloscope which is configured to trigger on the *B*-field probe signal as seen in figure 5. The scope trigger is then fed into a pulse generator which generates a trigger which is sent to the FPGA board used as part of the data acquisition (DAQ) system. General Purpose Interface Bus (GPIB) control of the pulse generator allows fine granularity trigger delays to be applied to the trigger, thereby allowing control of the phase of the triggers being sent to the module relative to the DC-DC switching. A trigger hold-off of 1 ms is set up on the scope so that data taking rates are limited to the 1 kHz rate that the current DAQ system can handle.

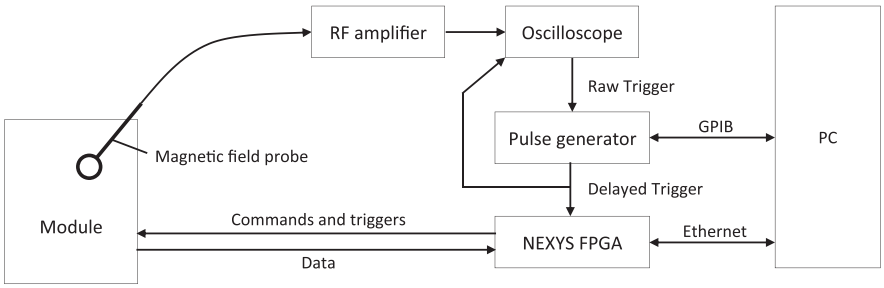

Figure 3. Schematic of the setup for running magnetic triggering tests on a module. Note that for the beam tests the GPIB communication between the PC and the pulse generator was not used.

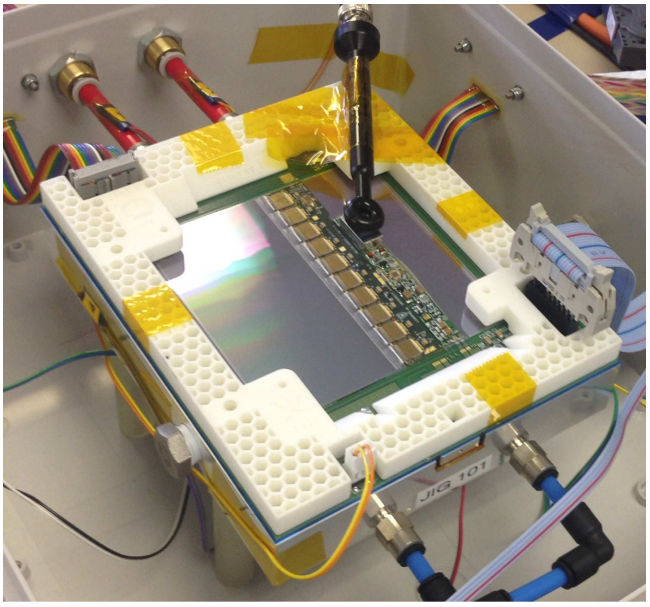

Figure 4. A module in a bench-top test box undergoing magnetic trigger testing. The magnetic field probe can be seen extending over the module from the top of the image.

As an alternative to using the fine granularity delay setting in the pulse generator, the latency configuration of the ABCstar can be scanned instead of the trigger delay. The latency configuration

2021 JINST 16 P06012

adjusts the length of the internal data pipelines and thereby allows coarse adjustment of the trigger phase relative to the DC-DC switching. Latency-based adjustment has a granularity defined by the bunch crossing frequency that the chips are designed for, in this case leading to a time step of 25 ns per count.

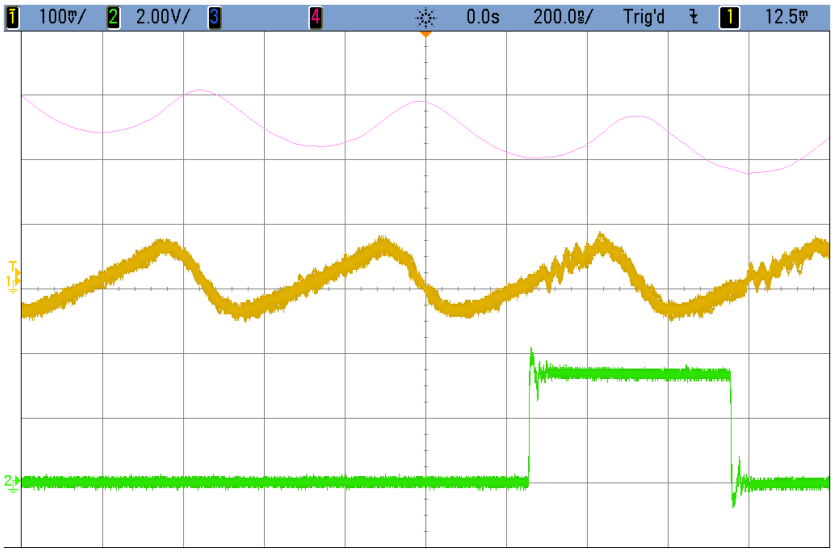

Figure 5. An oscilloscope plot taken during a magnetic triggering test. Channel 1 (yellow) shows the voltage signal coming from the magnetic field probe on which the scope triggers. Channel 2 (green) shows the trigger signal going from the pulse generator to the DAQ system. The purple trace is the integral of the signal from the magnetic field probe.

In the bench tests shown below, the pulse generator is used to provide the trigger delay in order to provide fine granularity timing control of 1 ns while for the beam tests below the latency-based coarse timing control is used. This is partly to simplify the setup and data taking process and partly due to the fact that the amount of beam time available was not sufficient to perform a fine granularity measurement.

Before running the full magnetic triggering scan, the module is trimmed to align the pedestals (corresponding to the amplifier offsets) of all channels. The trimming process ensures that the channel-by-channel response without charge injection is equalised across the module, and an asynchronous run is performed scanning the noise occupancy as a function of threshold. This stage is done using triggers generated internally by the DAQ system, fully independent of the magnetic triggering setup. Based on the obtained pedestal, a threshold for subsequent runs is chosen to correspond to approximately 50% occupancy. Next, an asynchronous run of 10 000 events at the selected threshold is performed using triggers generated by the pulse generator, but at a fixed frequency of 1 kHz, which is independent of the trigger coming from the scope. Finally, a synchronous scan of 10 000 triggers per step is performed at the selected threshold, varying the trigger delay from 0 to 1000 ns in steps of 1 ns. Note that in all the above cases, no charge is injected into the sensor and so any signal is, by definition, noise.

2021 JINST 16 P06012

Next, the results from both the asynchronous reference scan and the synchronous scans are normalised by the number of triggers to give a value of noise occupancy (NO), i.e. the occupancy depending on the applied readout threshold in the absence of an input signal. The synchronous NO is then normalised to the asynchronous NO in order to remove any plotting artefacts arising from remaining channel-by-channel variation in response. Figure 6 shows the results of this analysis for both strip segments (uncovered strips and strips located under the hybrid and powerboard). Significant features are seen between channels 600 and 950 on the strips running underneath the powerboard, which is the region where the DC-DC converter is located.

A repeating pattern is observed which has a period of around 500 ns, corresponding to the 2 MHz switching frequency of the DC-DC circuit. A repeating pattern, albeit of smaller magnitude, is also observed on strips not under the DC-DC converter and even on strips that do not run under the hybrid or powerboard. This suggests that not only is there significant signal injection occurring directly under the DC-DC converter but also that there is a movement of the reference levels across the module.

The measurements performed thus far have only dealt with the time-resolved measurement of the noise of the module. Of equal importance is the effect that this has on the measurements of real signals which therefore requires a time-resolved measurement which includes charge being injected into the sensor. Combining these two measurements will then allow the extraction of an expected signal-to-noise ratio which is the quantity used to quantify the final performance of the module.

3 Using an X-ray beam for magnetic triggering measurements

S-curves obtained in time-dependent measurements without input charge showed that the noise occupancy at a given threshold, i.e. noise, is dependent on the phase of the trigger relative to the switching of the DC-DC converter. This effect is observed primarily in the vicinity of a shield box and, to a lesser extent, across the whole module. The measurement showed that, while the average noise increase in channels under a powerboard shield box may be relatively small, it varies with phase and can be large for part of the latency range.

The ITk strip tracker was designed to ensure a minimum signal-to-noise ratio of 10:1 [1], with a worst case of about 12:1 (expected for modules located in a particular area of the detector's forward region at their end-of-life dose). A significant noise increase in a single part of a module could reduce the signal-to-noise ratio below the required minimum and affect the overall performance.

Therefore, follow-up measurements were performed using a monochromatic, micro-focused X-ray beam at the Diamond Light Source [6]: the injection of a known charge allowed a measurement of an additional S-curve to compare with S-curves obtained without input charge and to measure the time-dependent signal-to-noise ratio directly. Additionally, the use of a micro-focused beam with a diameter much smaller than the strip pitch ($2 \times 3\ \mu m^2$ compared to 75.5 µm) provided the possibility to focus on the centre of an individual strip and prevent charge-sharing in edge regions between adjacent strips. Different from setups utilising sources or particle beams, this measurement could therefore be configured to provide a precisely known input charge and reliable signal-to-noise ratio measurement.

2021 JINST 16 P06012

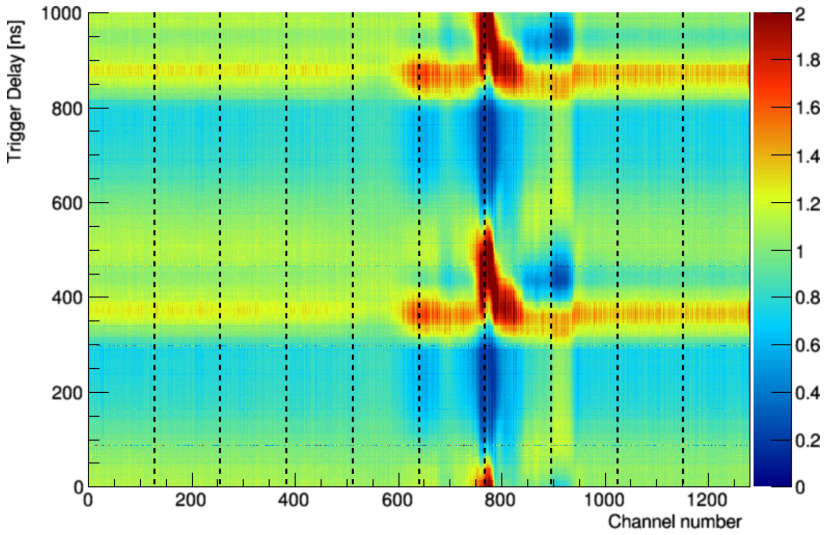

(a) Strips under hybrid and powerboard.

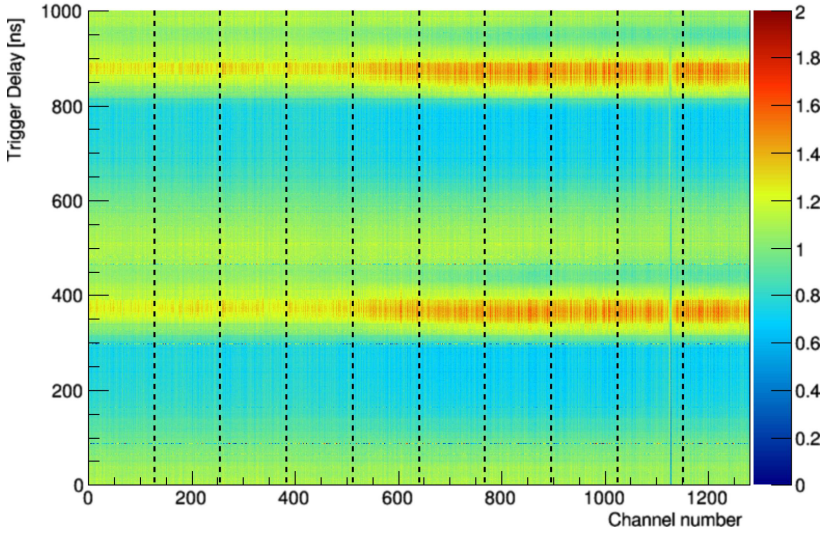

(b) Strips away from hybrid and powerboard.

Figure 6. Magnetic triggering result for a long strip module. Results are shown as a ratio of the synchronous noise occupancy to an asynchronous reference result. The threshold is selected to give ~50% occupancy in the asynchronous case. The powerboard approximately covers channels 0 to 940. Vertical dashed lines show the chip boundaries.

An X-ray beam with a photon energy of 15 keV was used. As the silicon sensors in use have a thickness of 300 µm, a 15 keV photon has a 51% chance of interaction, which leads to the production of one 15 keV electron. A single 15 keV electron travels up to 20 µm within silicon while producing 4200 electron-hole pairs, or a total input charge of 0.67 fC. This charge is equivalent to approximately 1/5 of the charge deposited by a MIP and therefore requires operation at a lower readout threshold.

2021 JINST 16 P06012

It should be noted that the high photon flux provided at the beamline (on average one photon interaction per 25 ns) would correspond to a 100% hit rate in a single module channel, while readout chips were designed for a maximum occupancy of 10%. As a result, the unattenuated X-ray beam was found to significantly alter the shape of the obtained S-curve (see figure 7). In order to allow a quantitative comparison of the module noise and S-curves with injected charge, magnetic triggering measurements were performed with an attenuated beam: aluminium attenuators with a combined thickness of 1.1 mm were used to reduce the beam intensity to 9.4%. As a result, the obtained S-curves were an overlay of events with and without photon interactions.

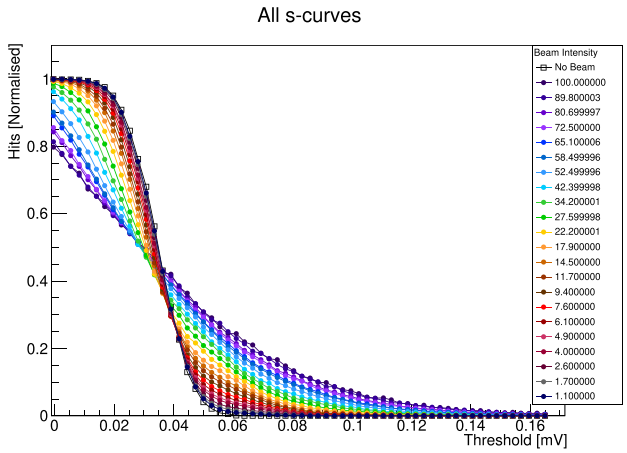

Figure 7. S-curves measured for one channel on a module for different beam intensities. While a lower beam intensity is expected to reduce the hit rate for high readout thresholds, beam intensities above 10% were found to also affect the S-curve at low readout thresholds.

4 Performing magnetic triggering measurements in an X-ray beam

Measurements were conducted using the same ABCStar long-strip module used for previous measurements using a magnetic field probe and oscilloscope to trigger synchronous data taking. The module was operated at a bias voltage of −350 V (fully depleted) inside a dry box which additionally served as a Faraday cage and shield against light. The box was flushed with nitrogen to prevent an early sensor breakdown caused by high humidity [7] and to stabilise the measurement temperature. Figure 8 shows the module in place at the beamline.

The module was mounted with the X-ray beam at a right angle to the sensor plane. Precision stages allowed movements of the module in x- and y-directions (perpendicular to the incoming beam and as defined in figure 1) with a positioning precision of O (µm). The module was oriented so that the sensor strips were parallel to the x-direction and perpendicular to the y-direction.

In preparation for the measurement, the alignment of the beam with respect to the strip implant was verified by moving the beam across a strip in 10 µm steps to find the edges of its charge collecting area. For magnetic trigger measurements with charge deposited by photons, the beam was pointed at the centre of the strip, where the strip implant was known to be located [8].

2021 JINST 16 P06012

Figure 8. The module in place at the beamline during coarse alignment. The opaque front of the test box has been removed. The data, power and magnetic field probe cables can be seen entering the box from the top with a nitrogen pipe (yellow) entering on the right. The magnetic field probe is taped in place over the module and the red horizontal laser alignment beam can be seen.

A given module channel under investigation was tested by performing a threshold scan from 0 to 40 DAC counts (corresponding to 0 – 111 mV) for a range of 31 latency settings (corresponding to a time delay of 0 to 750 ns in steps of 25 ns), which were later converted to one S-curve per latency setting. For each latency and threshold, 1000 triggers were sent, which resulted in a combined time of 20 min per module channel under investigation, i.e. per beam position on the module. Since a powerboard shield box covers a length of approximately 20 mm across the strips on a sensor (equivalent to 250 strips), a full scan of each individual channel would correspond to more than 80 hours of beam time. Therefore, instead of studying each channel individually, scans were performed only for every tenth strip, i.e. in steps of 755 µm, which was considered sufficiently small compared to the size of components on the powerboard.

In addition to providing a well-known photon signal and high positioning precision, the use of an X-ray beam provided the additional advantage of mapping the positions of module channels to powerboard features. While the exact position of components inside a shield box is usually unknown, the use of an X-ray allowed to map the positions of components inside the shield box

2021 JINST 16 P06012

using photon absorption: by moving the beam over a grid of positions matching the location of the shield box and measuring the resulting hit rate, the amount of material at that position could be deduced. Since the material on a powerboard is inhomogeneously distributed, the resulting hit map rate (see figure 10) could be used to associate observed impacts on a channel's S-curve with the location of features on the powerboard.

In order to map areas on the obtained hit map with corresponding powerboard areas, they were compared with an X-ray image of the same module area (see figure 9(a)), which was in turn compared to a photograph of a comparable area on another powerboard (see figures 9(b) and (c)).

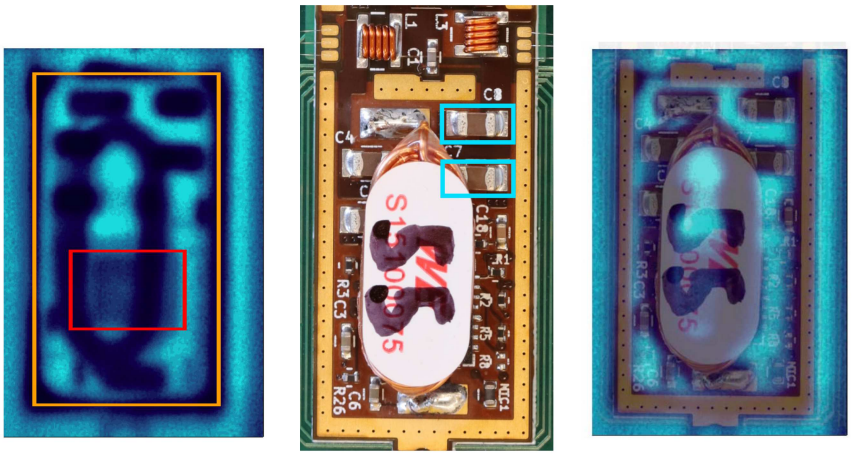

(a) X-ray image of shield box area

(b) Photograph of the shield box area of a powerboard

(c) Overlay of X-ray and visual image

Figure 9. Images used to map module readout channels to features on a powerboard. Since features were not visible through the closed shield box, an X-ray image was taken of the module under investigation and compared to the layout of a PCB without shield box. For comparison with the obtained hit map (see figure 10), the shield box position (orange), chip (red) and two SMD components (cyan) are highlighted.

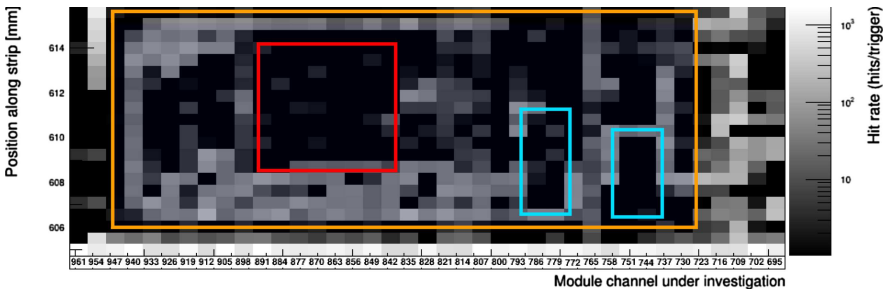

Figure 10. Hitmap for a coarse grid scan around the shield box area of a powerboard and corresponding module for each vertical line. Prominent features in the plot were compared to X-ray images of the same area to map module channels to powerboard features. The outline of the shield box (orange), the readout chip (red) and two SMD components (cyan) were marked for comparison with images shown in figures 9(a) and (b).

2021 JINST 16 P06012

5 Data analysis

Having performed a threshold scan with the beam centred on each channel under investigation, the occupancy as a function of threshold is calculated for when the beam is and is not incident on the strip. Afterwards, the difference between beam and no-beam threshold curves (the "noise-subtracted signal") is calculated. The results for a single representative strip are shown in figure 11.

Ideally "Vt50", the 50% occupancy point, would be extracted from the beam and no-beam results to perform the analysis. This is done for the no-beam case by fitting a complementary error function to the data. However, due to photon signals only being deposited for about 49% of events, Vt50 cannot be directly measured with beam. Instead, a proxy to Vt50 is calculated, using the difference between the occupancy with and without beam, the noise-subtracted signal occupancy. The Vt50 with beam is then defined as the threshold at which the noise-subtracted signal occupancy is 50% of the peak noise-subtracted signal occupancy, as calculated from a fit to the data. For example, in figure 11, the no-beam Vt50 is 12 DAC while the proxy Vt50 with beam is 24 DAC.

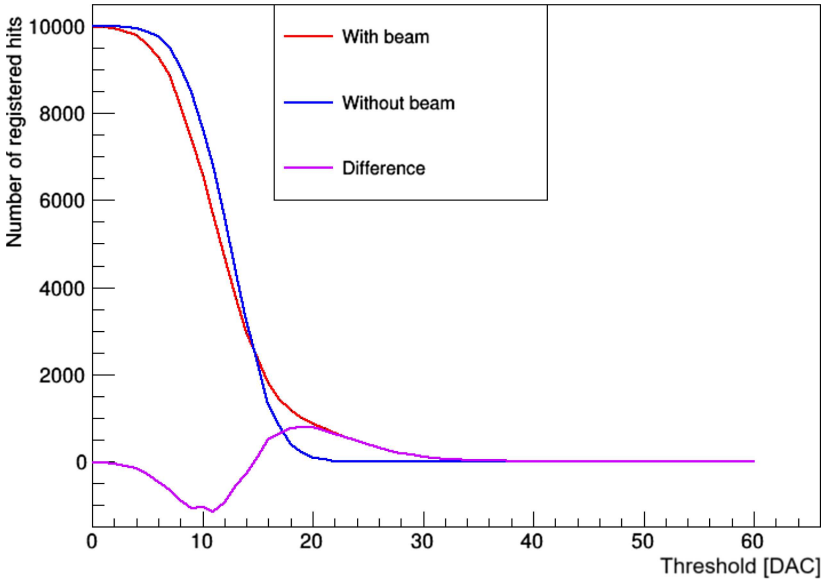

Figure 11. Representative example of signal curves (red), noise curves (blue) and noise-subtracted signal (magenta) as a function of threshold in DAC counts. The occupancy on the *y*-axis is given by the number of hits recorded in a sample of 10 000 triggers.

This analysis of occupancy as a function of threshold with and without beam is performed on all channels investigated (every tenth channel running under the DC-DC area of the powerboard) for a range of latency values. The variation of Vt50 as a function of channel and latency, with and without beam, is shown in figure 12, where the threshold DAC setting has been converted to threshold voltage using a calibration curve derived from analogue simulation of the front-end [9].

2021 JINST 16 P06012

Figure 12 shows similar features to those which have been measured in the laboratory and shown in figure 6. Although the average value of Vt50 changes with and without beam, as shown by the change in the mean z-axis value, the variation of Vt50 across channel and latency is almost identical with and without beam, suggesting that noise and signal S-curves move coherently within threshold space as a function of latency.

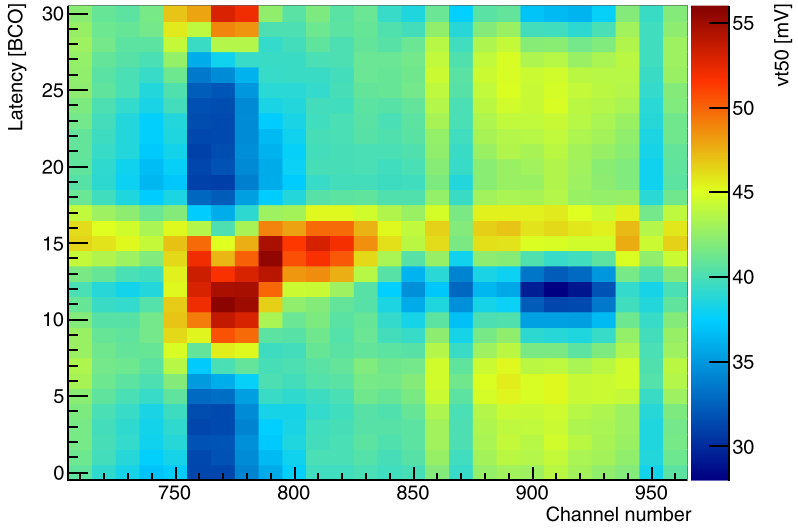

(a) Vt50 threshold measured without beam.

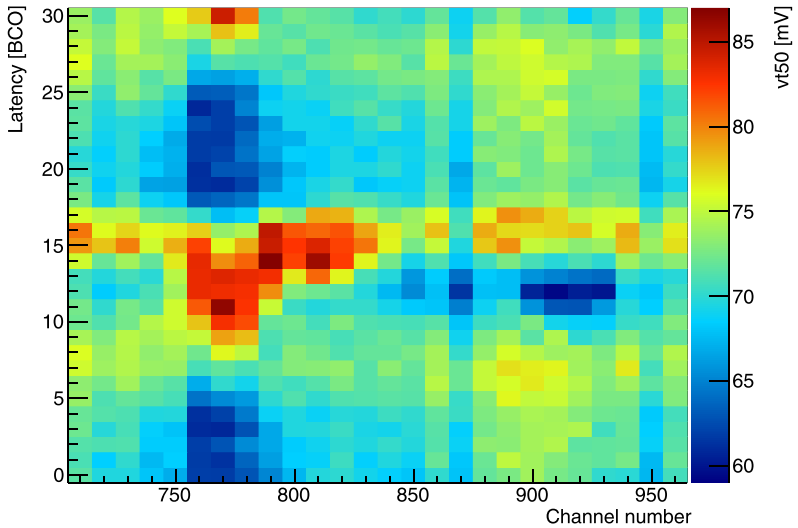

(b) Threshold at 50 % corrected maximum value (see figure 11) with beam on.

Figure 12. Shift of reference threshold with latency and strip number in the absence/presence of beam.

In addition to the Vt50 value, the width of the complementary error function used to fit the no-beam data can also be extracted. This provides a measurement of the noise of module as a

function of channel number and latency. This can be seen in figure 13. As can be seen, the noise varies dependent on the timing with respect to the DC-DC switching but there is significantly less variation in noise as a function of position on the module (channel number).

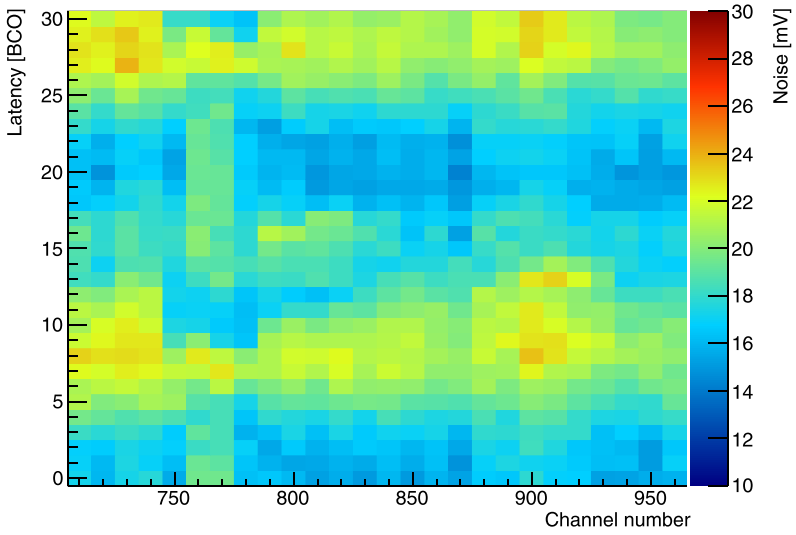

Figure 13. Noise as a function of channel number and latency.

6 Latency-resolved signal-to-noise ratio

In order to understand the effect of the measured time-resolved variation in Vt50 and noise has on the performance of the final detector, a model has been built to calculate efficiency and noise occupancy curves for a given noise and signal size. First, a noise occupancy curve is calculated based on the expected detector noise and assuming a Gaussian noise distribution. Next, the expected efficiency curve of the detector is built using:

$$\epsilon = 0.5 \times \texttt{erfc}\left[\frac{q_{\text{thr}} - \mu}{\sqrt{2}\sigma}\left(1 - 0.6\ \tanh\ \frac{\zeta(q_{\text{thr}} - \mu)}{\sqrt{2}\sigma}\right)\right] \tag{6.1}$$

where q_{thr} is the threshold, μ is the median charge where the occupancy is 50%, σ is the width of the error function and ζ is the skew of the function which takes account of the Landau tail.

Values for the skew and width are taken from test-beam measurements of prototype modules [10, 11]; the expected signal is taken from sensor measurements [12]. Values of 0.49 and 0.58 are used for the skew and width respectively while a noise of 625 (760) electrons and a signal of 10 183 (22 000) electrons is assumed at the end-of-life (start-of-life) of the detector. It should be noted that the end-of-life noise is less than the start-of-life as the detector will be run much colder at end-of-life and there is a significant dependence of the front end gain on temperature. The most probable value (MPV) of deposited charge used in the efficiency curve is based on the signal value above scaled by factors of 0.94 (1.11), which were again extracted from the test-beam measurements.

2021 JINST 16 P06012

Figure 14 shows the calculated efficiency and noise occupancy curves as a function of threshold for beginning and end-of-life of the detector. The design of the detector leads to requirements of at least 99% efficiency with no more than 10^{-3} noise occupancy throughout the life of the detector. As can be seen, this is easy to manage before radiation damage, but the operational window of the detector significantly decreases when radiation effects are taken into consideration at the end-of-life. The operational window is reduced to readout thresholds between the equivalent of 0.4 and 0.5 fC, compared to an MPV of the expected input charge of 1.63 fC (3.52 fC) at the end-of-life (start-of-life) of the detector.

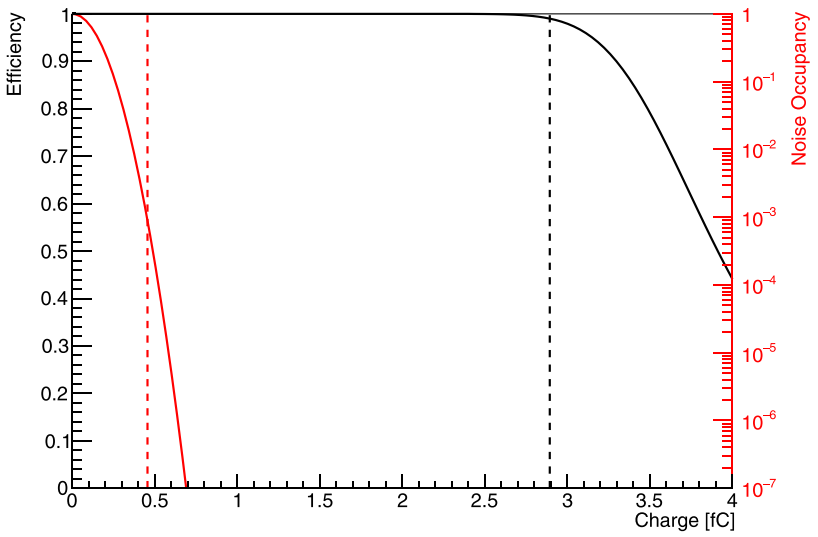

(a) Start-of-life

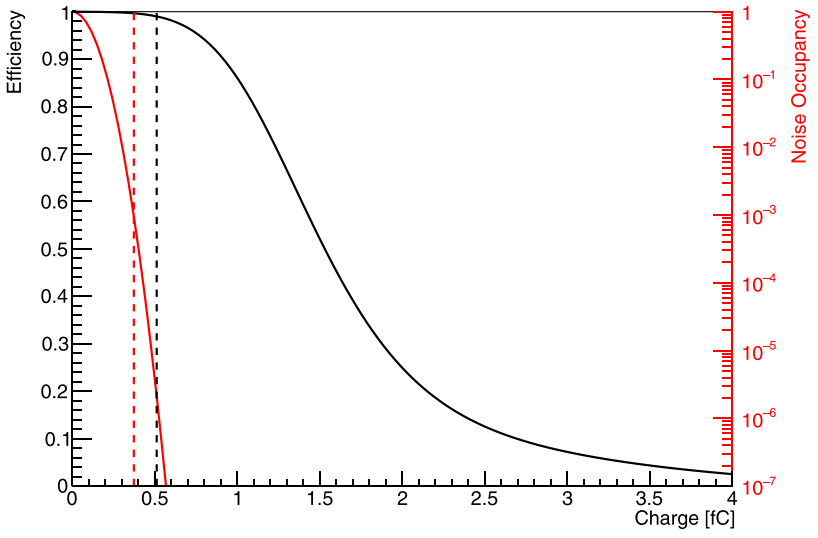

(b) End-of-life

Figure 14. Calculated efficiency (black) and noise occupancy (red) curves for a long strip module at the beginning of running and at the end of the lifetime of the experiment. The black and red dashed lines denote the required thresholds to satisfy 99% efficiency and 10^{-3} noise occupancy respectively. The operating window is the region above the red dashed line but below the black dashed line.

2021 JINST 16 P06012

In order to extrapolate the effects of the synchronous Vt50 and noise variations shown above, these efficiency and noise occupancy curves have been recalculated for each bin of channel number and latency. First, the efficiency curve is built and shifted in threshold by the amount which the Vt50 varies from the mean in figure 12, having restricted the calculation of the mean to a single period of the DC-DC. Given that the variation in the noise is small in comparison to the Landau width arising from the shape of the signal deposition in the sensor, the width of the efficiency curve is not varied from nominal.

Second, the noise occupancy curve is varied by scaling the noise used to build the noise occupancy by the amount of variation given in figure 13. In addition, the curve is shifted in threshold by the measured Vt50 variation in the same way as the efficiency curve above.

Having generated efficiency and noise occupancy curves for each bin of latency and channel number, a search is then performed for an operating window which could work in all bins. In other words, the highest threshold arising from the noise occupancy calculation is compared to the lowest threshold arising from the efficiency calculations. These are the two worst case scenarios and define the operating window once the time-resolved variations are taken into consideration.

The final operating window result is shown in figure 15 which shows the nominal calculated efficiency and noise occupancy along with curves for all of the latency and channel number bins. As can be seen, the previously small operating window from figure 14 has completely disappeared once the time-resolved variation has been taken into consideration and the 99% efficiency working point is now at 0.35 fC while the 10^{-3} noise occupancy working point is above this at 0.6 fC. The demonstrated approximation of time-resolved end-of-life module performance based on a combination of X-ray and electron beam tests suggests that further optimisation of the powerboard geometry may be necessary to achieve the intended end-of-life module performance. For a conclusive statement about the necessity of further modifications, additional measurements with modules irradiated to their end-of-life fluence and dose are planned to be conducted.

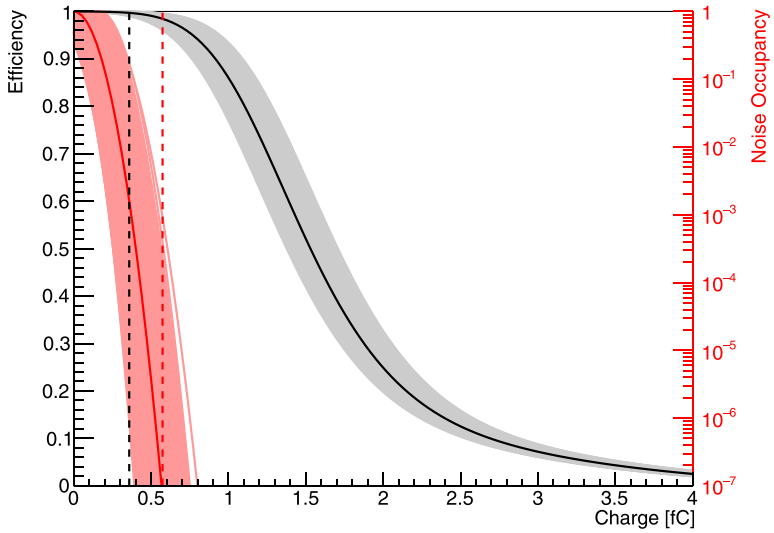

Figure 15. Calculated efficiency (black) and noise occupancy (red) curves for a long strip module at the end-of-life. Solid lines show the nominal calculation, lighter lines show the calculated curves for every latency and channel bin individually. The black and red dashed lines denote the required thresholds to satisfy 99% efficiency and 10^{-3} noise occupancy respectively in all latency bins. The black dashed line being below the red dashed line demonstrates the lack of an operating window.

2021 JINST 16 P06012

7 Conclusion and outlook

In this paper, a novel method for investigating the effects of DC-DC converters in the presence of silicon strip sensors has been presented, whereby module characterisation is performed synchronously with the switching of the DC-DC converter. This technique has been used to study synchronous effects of the DC-DC switching on both the noise and signal efficiency of the detector. This thereby allows the measurement to be made of the signal-to-noise ratio as a function of phase relative to the DC-DC switching.

In addition, a toy model of the end-of-life performance of the detector has been built using measurements performed at test-beam. Using this model, the synchronous effects measured are extrapolated to end-of-life and demonstrate the degree to which a baseline (Vt50) shift as measured here can affect the operating window of the final detector.

The measurements shown here were taken at room temperature on a module before irradiation and then extrapolated to end-of-life. In order to fully understand the effect on the operating window, these measurements should be repeated with irradiated modules at end-of-life operating temperatures. The measurements should also be repeated on the other types of modules used in the experiment, particularly end-cap modules employing radial strips and short strip modules where the powerboard straddles the two strip segments.

Finally, as demonstrated in this paper, when investigating the effect of DC-DC converters in the presence of silicon detectors, characterisation should be performed both asynchronously and synchronously to the DC-DC switching frequency. Synchronous data taking has the ability to shed light on the exact time structure of EMI noise injection into the sensor and is also required to demonstrate that the detector not only satisfies specifications when averaging across the DC-DC cycle but also satisfies specifications at all phases relative to the DC-DC switching.

Acknowledgments

This work was supported in part by the U.S. Department of Energy, Office of Science, High Energy Physics, under Contract No. DE-AC02-05CH11231, the USA Department of Energy, Grant DESC0010107, the Canada Foundation for Innovation, the Natural Sciences and Engineering Research Council (NSERC) of Canada as well as the Alexander von Humboldt Foundation and the Science and Technology Facilities Council, UK. We acknowledge the Diamond Light Source for time on beamline B16 under proposal MT22002. The authors would like to thank the personnel of the B16 beam, especially Oliver Fox and Andy Malandain, for providing advice and support during the experiment.

References

[1] The ATLAS collaboration, *Technical design report for the ATLAS inner tracker strip detector* Technical Report CERN-LHCC-2017-005, ATLAS-TDR-025 CERN, Geneva 2017.

[2] L. Poley et al., *The ABC130 barrel module prototyping programme for the ATLAS strip tracker,* 2020 *JINST* **15** P09004.

2021 JINST 16 P06012

[3] S. Michelis et al., *DC-DC converters in 0.35 μm CMOS technology,* 2012 *JINST* **7** C01072.

[4] K. Cormier et al., *Development of the front end amplifier circuit for the ATLAS ITk silicon strip detector,* submitted to *JINST.*

[5] Y. Unno et al., *ATLAS17LS — a large-format prototype silicon strip sensor for long-strip barrel section of ATLAS ITk strip detector,* *Nucl. Instrum. Meth.* A **989** (2021) 164928.

[6] K.J.S. Sawhney et al., *A test beamline on Diamond Light Source,* *AIP Conf. Proc.* **1234** (2010) 387–390.

[7] J. Fernández-Tejero et al., *Humidity sensitivity of large area silicon sensors: study and implications,* *Nucl. Instrum. Meth.* A **978** (2020) 164406.

[8] L. Poley et al., *Characterisation of strip silicon detectors for the ATLAS phase-II upgrade with a micro-focused X-ray beam,* 2016 *JINST* **11** P07023.

[9] J. Kaplon and M. Noy, *Front end electronics for SLHC semiconductor trackers in CMOS 90 nm and 130 nm processes,* *IEEE Trans. Nucl. Sci.* **59** (2012) 1611–1620.

[10] E. Rossi, *Characterization of silicon modules and sensors for the ATLAS inner tracker strip detector,* Ph.D. Thesis, Universität Hamburg, Hamburg (2020).

[11] F. Rüehr et al., *Testbeam studies of barrel and end-cap modules for the ATLAS ITk strip detector before and after irradiation,* *Nucl. Instrum. Meth.* A **979** (2020) 164430.

[12] K. Hara et al., *Charge collection study with the ATLAS ITk prototype silicon strip sensors ATLAS17LS,* *Nucl. Instrum. Meth.* A **983** (2020) 164422.

2021 JINST 16 P06012